Alma Mater Studiorum

Physics of Medical Imaging

Monte Carlo simulation of gamma camera in different geometries

Leonardo Conti

Simone Santoro

Mohammad Zain

Academic Year: 2023/2024

Contents

Chapter 1

Introduction

The aim of this experiment is to study the behaviour of the sensitivity and spatial resolution of a gamma camera in different geometric configurations using Monte Carlo simulations. The parameters that, in this experiment, differ from one simulation to the other, are mostly related to the shape of the collimator and the detector, but also to the position of the photon source.

It is therefore crucial that the basic concepts about the gamma camera and it's main components, as well as Monte Carlo method, are introduced. Purpose of this chapter is to provide the reader with that knowledge.

1.1 Gamma Camera

The gamma camera, also known as Anger camera, is a medical apparatus for diagnostic applications in the context of nuclear imaging. By exploiting the scintigraphy technique, it is able to detect photons produced by radioisotopes injected in the patient body. Signal obtained from the detection system is then processed to create the 2D image of the region of interest. The description of the signal processing, as well as the components of the gamma camera related to the signal amplification, are out of the scope of this report.

Therefore, by simplifying the structure of the gamma camera, it can be stated that it is composed of a collimator and a scintillator detector.

1.1.1 Collimator

The collimator of a gamma camera determines the direction at which an incoming photon is able to reach the detector, while absorbing most of the others. Therefore, it is typically made with high Z materials, usually lead. The most used type of collimator, also the one used in this experiment, is the parallel hole collimator, containing a large number, usually thousands, of parallel holes. Such holes can have different geometries. In this experiment, hexagonal holes were chosen, as they represent the state of the art in most cases. The partitions between the holes are called septa, and they're thickness, as well as the hole size, is an important geometric parameter for a collimator. The septa thickness, in fact, determines the maximum energy of photon for which a collimator can be used, distinguish Low energy collimators (up to $150 keV$) from High energy collimators (up to $400\ keV$).

As will be further discussed in the following sections, there is an important connection between septa thickness and hole size: for a given collimator size, increasing the hole size means decreasing the septa and vice-versa. Intuitively, the bigger the holes, the more photos are able to pass trough, and, therefore, the higher the efficiency in the photon detection. Conversely, the smaller the septa thickness, the more photons are able to cross the collimator material, resulting in the decreasing of the resolution.

1.1.2 Detector

The detector is the actual core of a gamma camera, being the crystal material able to interact with incoming photons and generate a signal that can be acquired. In the context of the gamma camera simulated in this experiment, the signal consists in the production of visible light after the scintillation process. Typical materials used as detectors are characterized by having high stopping power and short decay time. High stopping power is necessary for having high detection efficiency, while the short decay time is crucial for the high count rate. A popular choice for the scintillator crystal is NaI(Tl).

1.1.3 Sensitivity

The sensitivity for a gamma camera is defined as follows:

$$\text{sensitivity} = \frac{\text{Number of detected photons}}{\text{Number of photons emitted}} \tag{1.1}$$

Under the assumption that all the photons passing trough the collimator are detected, it is possible to define the geometric sensitivity G as:

$$G = \frac{\text{Number of photons passing trough collimator}}{\text{Number of photons emitted}} \tag{1.2}$$

It can be derived that the geometric sensitivity for a parallel hole collimator is proportional to it's the geometric properties according to:

$$G \approx \frac{d^4}{12l^{12}\left(d+t\right)^2} \tag{1.3}$$

1.1.4 Resolution

Spatial resolution gives information about the level of detail that can be achieved in the image. In case of a parallel hole collimator, the spatial resolution can be approximated as follows:

$$\delta r \approx d\frac{l+z}{l} \tag{1.4}$$

And, in case of a point-like source of photons, the collimator resolution can also be estimated in terms of Full Width Half Maximum (FWHM) of the Point Spread Function. The PSF, as the name suggests, is the response of the detection system to the point input. In case of isotropic detector response, achieved when the PSFs

along the two transversal axes of the detector are the same, the resulting PSF is a Gaussian shaped 2D function. It's FWHM, obtained by using:

$$FWHM = 2.3548\sigma \tag{1.5}$$

Where σ is the variance of the PSF. The relationship between the PSF and spatial resolution is evident when examining the relationship between the former, the line spread function (LSF(x)) and the modulation transfer function (MTF(f))[1]:

$$LSF(x) = \int_{y=-\infty}^{\infty} PSF(x,y)dy$$

$$MTF(f) = |FT(LSF(x))| = \left| \int_{x=-\infty}^{\infty} LSF(x)\exp{(-2\pi ifx)}dx \right|$$

Where $FT(LSF(x))$ stands for the Fourier transform of $LSF(x)$. If the spatial resolution is understood to be the distance corresponding to the frequency value f_t for which $MTF(f_t)$ is lower than some threshold value T (for example $T = 0.1 * MTF(0)$), then it can be seen that an $LSF(x)$ significantly different from 0 in a wider range of values would bring to a narrower MTF and therefore the f_t frequency will have a lower value therefore increasing that of δr.

The visible light photons, during their travel to the PMTs, spread out according to the direction of emission: it is apparent that the longer the distance they need to travel, the greater the deviation from the original radiation direction will be. It will be determined in *Chapter [3]* that the visible light causes a reduction of the spatial resolution, resulting in a blurring effect in the output image.

1.2   Monte Carlo Method

The Monte Carlo method is a well known numerical approach to problems which are difficult to solve analytically. Specifically, is consists in a statistical approach that exploits random numbers for simulating any specified situation. Being a numerical approach, there is no need for the exact equation describing the system behaviour. In order for the Monte Carlo method to work, however, the system, as well as the possible interactions that modify it's state, need to be expressed as probability density functions (pdfs). Once the pdfs are known, the algorithm samples them and computes the result, repeating the process for a sufficiently large number of times to reduce statistical error.

In the context of radiation transport, the Monte Carlo algorithm needs to be provided with the exact geometry to simulate, defining the boundaries separating different materials, and the materials cross sections for radiation interaction, representing the probabilities for all the possible interactions.

Chapter 2

Materials and Methods

In this study, Monte Carlo simulations were performed to analyze the spatial resolution and sensitivity of a gamma camera in different geometric configurations. This chapter aims to provide a detailed explanation of both the experimental setup and the data analysis pipeline.

2.1 Experimental setup

The experimental setup includes a gamma camera and a source of photons placed in a vacuum. The gamma camera geometry, as well as the distance of the source were considered in different configurations. Regarding the gamma camera, it is made by connecting a collimator to a scintillator layer, each with different geometric characteristics. Three different collimators were considered, named A, B and C, all of them being parallel-hole collimators with hexagonal holes and frontal area of $10 \times 10 \ cm^2$. The exact values of the geometric characteristics are reported in the following table.

Collimator	Hole Diameter (mm)	Septa Thickness (mm)	Collimator Thickness (mm)	Diameter over C. Thickness
A	3.0	0.3	25.0	0.12
B	1.5	0.3	15.0	0.10
C	1.5	0.2	22.0	0.07

Table 2.1: Table representing, for each collimator, the hole diameter, septa thickness, collimator thickness and the ratio between hole diameter and collimator thickness

Each collimator was used in combination with a scintillator layer, also having frontal area of $10 \times 10 \ cm^2$, made of NaI(Tl). The thickness of the scintillator was varied between $2mm$ and $10mm$.
The source, emitting for each simulation 10 million photons with an energy of $140kev$, was considered to be a 3D cylindrical source centered in the middle of the gamma camera at three different distances: $5cm, 10cm,$ and $15cm$.
Therefore, 18 different configurations were considered and simulated; For each of them, the PSF was estimated both considering and neglecting the blurring effect

caused by the emission of visible light in the scintillator layer.

Additionally, the sensitivity of the camera was computed as the ratio between the number of detected photons and the number of photons emitted from the source.

2.2 Data acquisition

For the simulation, we employed the EGSnrc distribution of the EGS (Electron Gamma Shower) Monte Carlo software, which is widely used for modeling the interaction of particles with matter. This software allowed us to accurately simulate the behavior of photons within the gamma camera setup.

Each one of the 18 different configuration was simulated 10 times, in order to associate a statistical uncertainty to the estimated quantities. The output of the EGS software consists in a .hsb binary file from which an n-tuple was obtained. Each column of the n-tuple represent one of the following quantities:

- Number of particles fired;

- Simulation history;

- Position of the emitted photons (x, y, z);

- Direction of emission (Direction Cosines);

- Energy deposition spectrum;

- Position of interaction neglecting visible light (x, y, z);

- Detected position of interaction considering visible light (x, y).

The output files regarding a particular geometric configuration were saved in a repository named according to the following convention:

"*geom_<Source-Distance>_<Scintillator-Thickness>_<Collimator-Geometry>*"

2.3 Data analysis

Data analysis was performed using MATLAB, enabling detailed examination and visualization of the results obtained from the simulations. The MATLAB script, consisting in a modified version of the one provided by Professor Lanconelli, as well as the data acquired, can be found on GitHub at the following link:

[GitHub Repository](#).

The aim of the simulations was to estimate both the sensitivity and the spatial resolution. The former, was computed according to *Equation [1.1]*, while the latter was expressed in terms of Full Width at Half Maximum (FWHM) of the Point Spread Function (PSF). The FWHM was evaluated according to *Equation [1.5]*. Where σ is the variance of the interaction points distribution, computed by fitting the histograms of either the x or y interaction positions with a Gaussian distribution, obtaining an estimate for the PSF.

This equation, however, is a valid estimate for a detector PSF only when it is

isotropic and therefore, to verify this property, Bartlett's test [3] was performed (see *Appendix B*). The aim of the test was to determine whether the values of the FWHM, calculated either using the x or the y interaction positions, were computed from distributions having the same variance: $\sigma_x = \sigma_y = \sigma$.

For the aforementioned validity reasons, distributions which were considered anisotropic under Barlett's test have been excluded from the averaging; This evaluation led to the resulting PSFs presented in chapter [3].

Additionally, the results obtained by averaging the non rejected PSFs were fitted with a linear function, both versus the ratio diameter over thickness and versus the source distance. The fits were performed both considering and neglecting the visible light production, to compare the results and propose an explanation to the effect that this light has on the final image.

Chapter 3

Results

The main results of the study will now be presented. In all of the following plots, each scintillator thickness-source_distance combination is represented by using a unique colour, and the results are grouped by their respective geometry. Each data point in the plots is the result of the average of the non-rejected measurements.

3.1 Sensitivity

The sensitivity, as mentioned in *Section [2.1]*, was estimated as the number of detected photons divided by the total number of photons emitted. *Figure [3.1]* shows a plotting of the sensitivities expressed as parts per thousand. The standard deviation (see *Table [3.1]*) is such that even at 95% confidence interval the error bars would be comparable to each column outline thickness: they are therefore not shown.
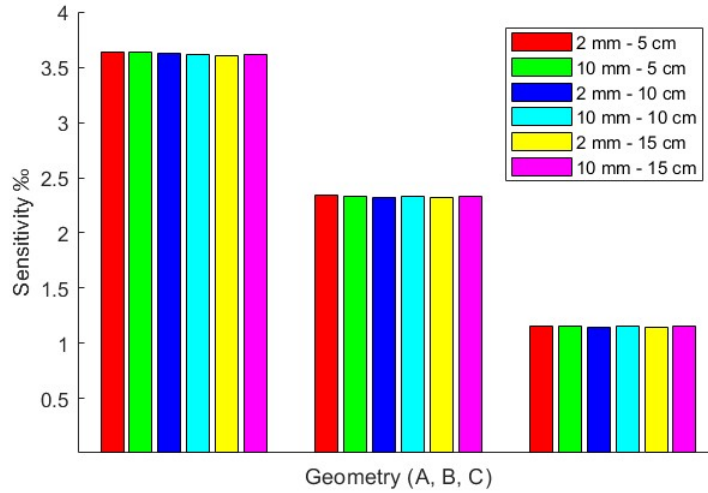

Figure 3.1: Plotting of the sensitivity of the various system configurations as parts per thousand. The data is grouped with respect to the collimator geometry (first group A, second group B and third group is C). Data points are represented as columns for easier qualitative evaluation.

	A	B	C
2 mm - 5 cm	(0.364 ± 0.001) ‰	(0.234 ± 0.001) ‰	(0.116 ± 0.001) ‰
10 mm - 5 cm	(0.364 ± 0.002) ‰	(0.233 ± 0.001) ‰	(0.116 ± 0.001) ‰
2 mm - 10 cm	(0.363 ± 0.003) ‰	(0.2326 ± 0.0008) ‰	(0.115 ± 0.001) ‰
10 mm - 10 cm	(0.362 ± 0.002) ‰	(0.234 ± 0.002) ‰	(0.116 ± 0.001) ‰
2 mm - 15 cm	(0.360 ± 0.002) ‰	(0.232 ± 0.001) ‰	(0.1146 ± 0.0009) ‰
10 mm - 15 cm	(0.361 ± 0.002) ‰	(0.233 ± 0.002) ‰	(0.1152 ± 0.0007) ‰

Table 3.1: Table of the computed values for the sensitivity and respective standard deviation for each combination of collimator geometry, scintillator thickness (given in mm) and source distance (given in cm)

3.2 Point Spread Function Estimates

The results of the PSF estimates are now presented. In *Tables [3.3]* and *[3.2]* are reported the number of rejected distributions for each geometric configuration respectively considering and neglecting the effects of visible light. In *Appendix [A]* the average p-values for the various system configurations can be inspected.

	A	B	C
2 mm - 5 cm	3	1	5
10 mm - 5 cm	1	1	2
2 mm - 10 cm	1	0	1
10 mm - 10 cm	1	1	0
2 mm - 15 cm	0	0	0
10 mm - 15 cm	0	1	1

Table 3.2: Number of rejected distribution for each system's configuration while **not** taking into account the effect of visible light

	A	B	C
2 mm - 5 cm	3	1	3
10 mm - 5 cm	1	1	2
2 mm - 10 cm	1	0	1
10 mm - 10 cm	1	1	0
2 mm - 15 cm	0	0	0
10 mm - 15 cm	0	0	1

Table 3.3: Number of rejected distribution for each system's configuration while taking into account the effect of visible light

The plots of the computed FWHM averages, evaluated from the isotropic distributions, can be seen in *Figures [3.3]* and *[3.2]*, respectively considering and neglecting the effect caused by visible light. For analogous reasons to the ones explained in the previous section, the standard deviations have not been represented, but can still be inspected in *Tables [3.4]* and *[3.5]*.
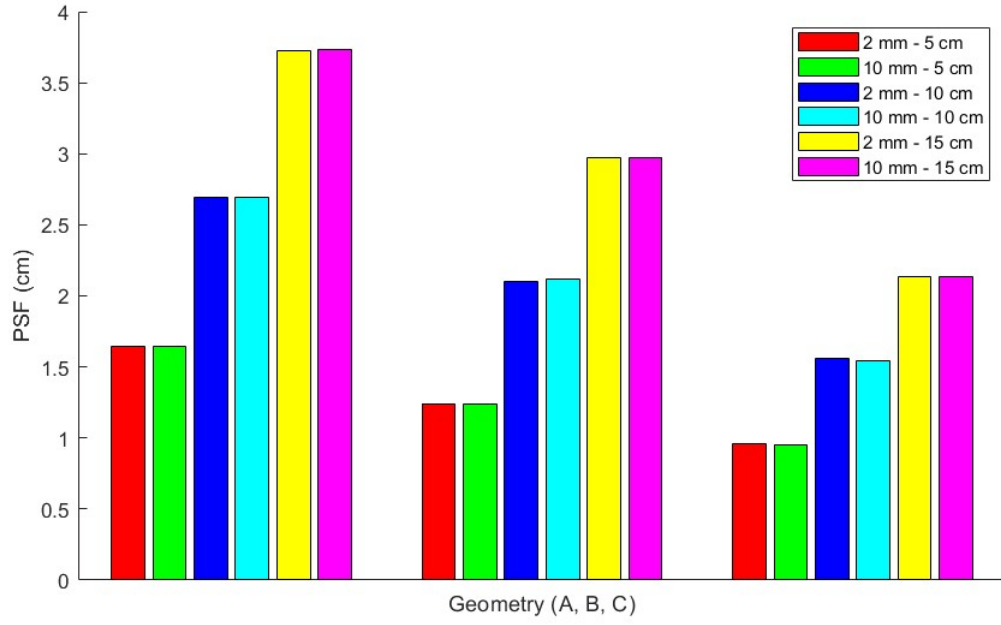
Figure 3.2: Plotting of the mean estimated PSFs for all the configurations grouped by the same convention as previous figures when **not** considering the effects of visible light.
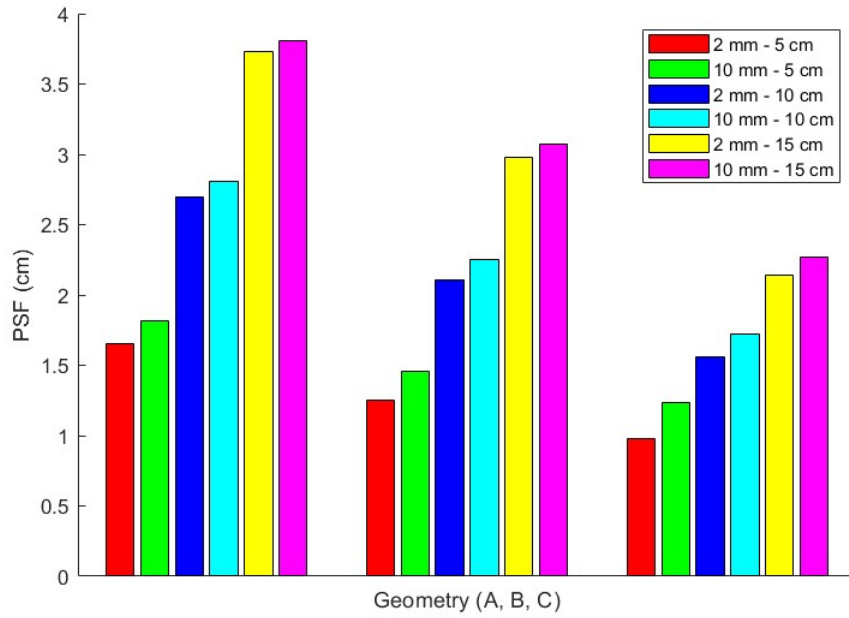

Figure 3.3: Plotting of the mean estimated PSFs for all the configurations grouped by the same convention as previous figures when considering the effects of visible light.

	A	B	C
2 mm - 5 cm	(1.643 ± 0.006) cm	(1.242 ± 0.009) cm	(1.16 ± 0.01) cm
10 mm - 5 cm	(0.96 ± 0.01) cm	(1.237 ± 0.008) cm	(0.96 ± 0.01) cm
2 mm - 10 cm	(2.695 ± 0.009) cm	(2.11 ± 0.01) cm	(1.556 ± 0.008) cm
10 mm - 10 cm	(2.70 ± 0.01) cm	(2.115 ± 0.008) cm	(1.54 ± 0.01) cm
2 mm - 15 cm	(3.73 ± 0.01) cm	(2.97 ± 0.01) cm	(2.13 ± 0.01) cm
10 mm - 15 cm	(3.73 ± 0.01) cm	(2.97 ± 0.01) cm	(2.14 ± 0.02) cm

Table 3.4: Table of the mean estimated PSFs and respective standard deviation for all the configurations organized by the same convention as previous tables when **not** considering the effects of visible light.

	A	B	C
2 mm - 5 cm	(1.651 ± 0.006) cm	(2.34 ± 0.01) cm	(1.250 ± 0.009) cm
10 mm - 5 cm	(0.98 ± 0.01) cm	(1.457 ± 0.007) cm	(1.231 ± 0.007) cm
2 mm - 10 cm	(2.699 ± 0.009) cm	(2.11 ± 0.01) cm	(1.563 ± 0.007) cm
10 mm - 10 cm	(2.80 ± 0.01) cm	(2.254 ± 0.007) cm	(1.73 ± 0.01) cm
2 mm - 15 cm	(3.73 ± 0.01) cm	(2.98 ± 0.01) cm	(2.14 ± 0.01) cm
10 mm - 15 cm	(3.81 ± 0.01) cm	(3.08 ± 0.01) cm	(2.27 ± 0.02) cm

Table 3.5: Table of the mean estimated PSFs and respective standard deviation for all the configurations organized by the same convention as previous tables when considering the effects of visible light.

Again, in *Appendix [A]* tables which present the values for the computed FWHM when the PSF is deemed anisotropic can be found.
By inspecting the two previous plots it is reasonable to assume that the PSF is weakly dependent on the scintillator thickness (more in *Chapter [4]*) and that it mostly depends on the collimator geometry (see *Figures [3.4]* and *[3.5]*) and the source distance (see *Figures [3.6]* and *[3.7]*): this dependency was quantified via linear regrssion in the two following sections.

3.2.1 Collimator geometry analysis

The dependency of the PSF on the collimator geometry is explored by fitting it versus the ratio between hole diameter and collimator thickness, while considering the same combination of scintillator thickness and source distance. When plotting the fits for the PSFs without taking light into consideration, the lines obtained for different scintillator thickness would overlap. Therefore, only the ones related to the 2 mm thickness are shown. The fitting lines have been forced to go through (0,0) since it is expected that, given a hole size equal to 0 cm and neglecting the photons that would pass through, no photon arrives at the scintillator and therefore there would not be an interaction position distribution. The angular coefficients obtained can be inspected in *Tables [3.6]* and *[3.7]*.
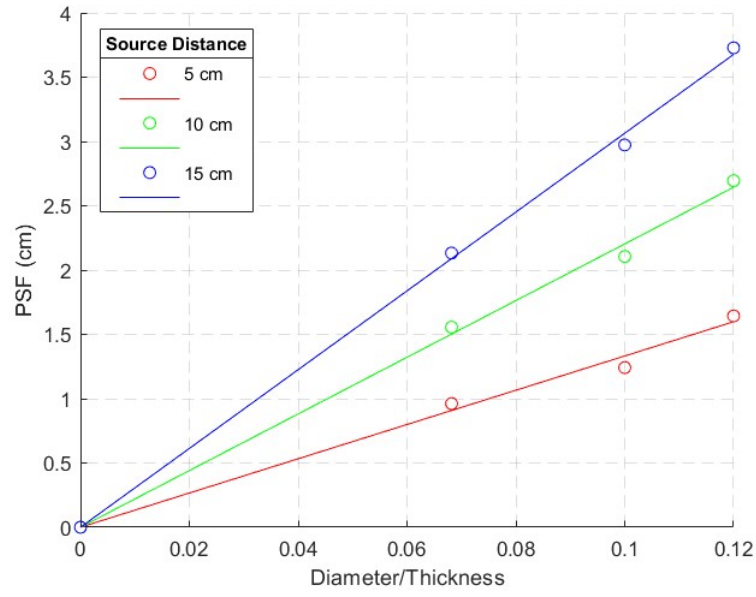
Figure 3.4: Best fit line for the PSF over the ratio between hole diameter and collimator thickness for different source distance. Production of visible light was neglected
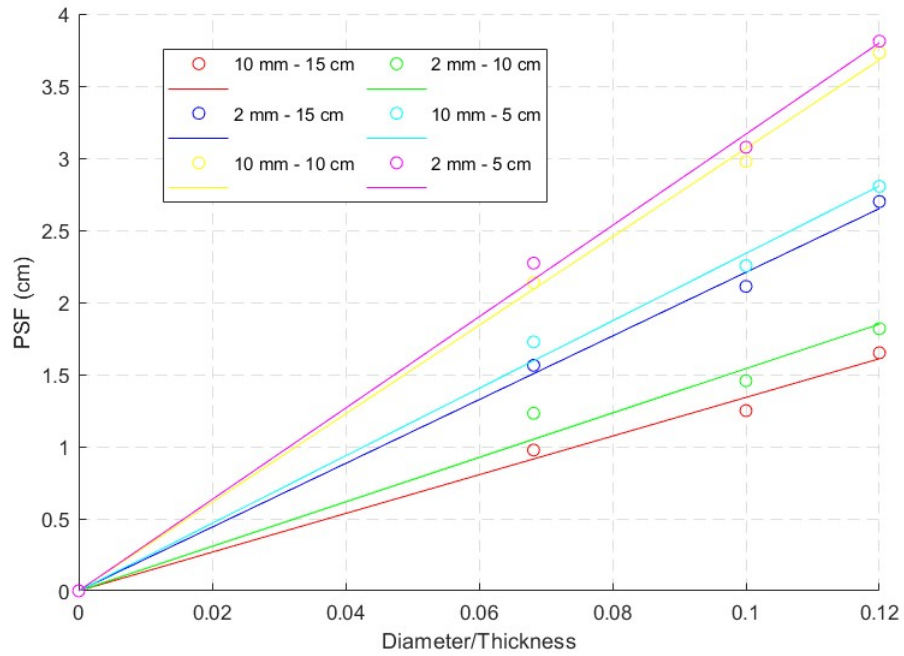

Figure 3.5: Best fit line for the PSF over the ratio between hole diameter and collimator thickness for different source distance considering the production of visible light

	2 mm	10 mm
5 cm	(13.3 ± 0.4) cm	(13.3 ± 0.4) cm
10 cm	(22.0 ± 0.4) cm	(22.0 ± 0.4) cm
15 cm	(30.6 ± 0.4) cm	(30.7 ± 0.4) cm

Table 3.6: Table of the estimated angular coefficient and respective standard deviation for all the configurations when **not** considering the effects of visible light. Source distance is given in cm and scintillator thickness is given in mm

	2 mm	10 mm
5 cm	(13.4 ± 0.4) cm	(15.4 ± 0.7) cm
10 cm	(22.1 ± 0.4) cm	(23.4 ± 0.5) cm
15 cm	(30.7 ± 0.4) cm	(31.7 ± 0.5) cm

Table 3.7: Table of the estimated angular coefficient and respective standard deviation for all the configurations when considering the effects of visible light. Source distance is given in cm and scintillator thickness is given in mm

3.2.2 Source distance analysis

The dependency on the source distance is studied by linear fitting the PSFs obtained with the same collimator geometry and scintillator thickness with varying source distance. Again, since the plots would overlap, when neglecting visible light only the lines obtained from a scintillator thickness of 2 mm are shown. For this analysis, since an intercept greater than 0 would have a physical interpretation (see *Chapter [1]*), the condition of passing through (0,0) is not imposed. The angular coefficients and intercepts obtained can be inspected in *Tables [3.8]* and *[3.9]*. In this analysis the (dimensionless) angular coefficient will be denoted by m and the intercept, given in cm, will be denoted by q
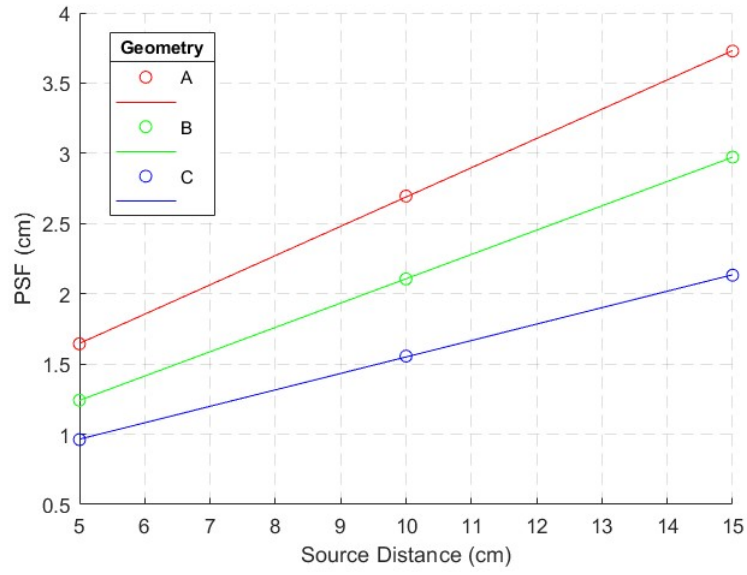
Figure 3.6: Best fit line for the PSF over the source distance for different geometries and scintillator thickness of 2 mm. Production of visible light was neglected
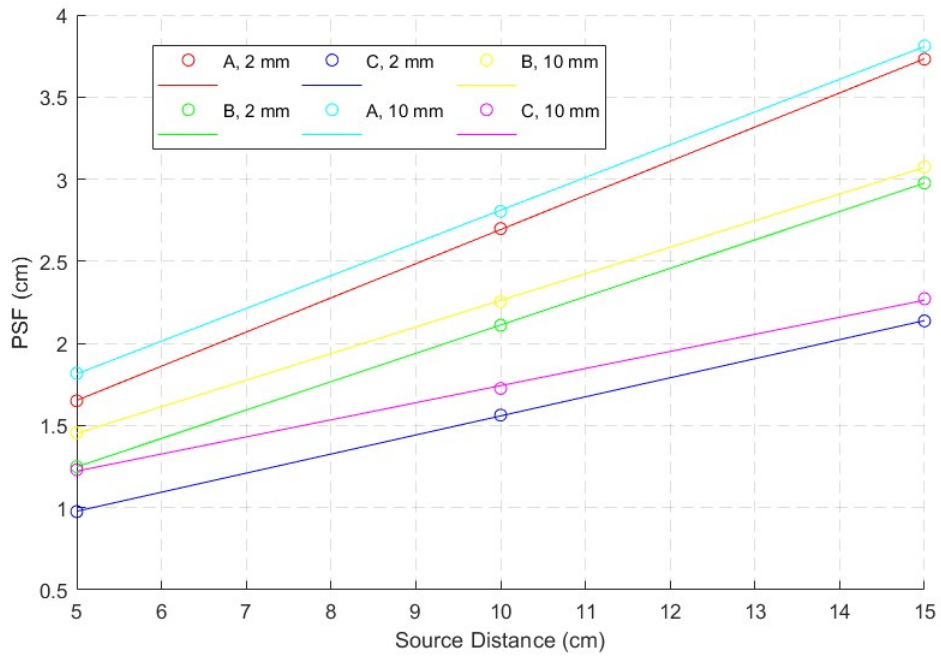

Figure 3.7: Best fit line for the PSF over the source distance for different geometries. Production of visible light was considered

	2 mm	10 mm
	m , q (cm)	m , q (cm)
A	(0.209± 0.001),(0.60±0.01)cm	(0.209±0.001),(0.61±0.01)cm
B	(0.1731± 0.0002),(0.376±0.002)cm	(0.174±0.001),(0.37±0.01)cm
C	(0.1171± 0.0001),(0.38±0.01)cm	(0.1181±0.0002),(0.365±0.002)cm

Table 3.8: Table of the estimated angular coefficient and respective standard deviation for all the configurations when **not** considering the effects of visible light. Source distance is given in cm and scintillator thickness is given in mm

	2 mm	10 mm
	m , q (cm)	m , q (cm)
A	(0.209± 0.001),(0.61±0.01)cm	(0.199±0.001),(0.82±0.01)cm
B	(0.1727± 0.0002),(0.385±0.003)cm	(0.162±0.001),(0.64±0.01)cm
C	(0.1161± 0.0008),(0.398±0.009)cm	(0.104±0.003),(0.70±0.03)cm

Table 3.9: Table of the estimated angular coefficient and intercept and respective standard deviations for all the configurations when considering the effects of visible light. Source distance is given in cm and scintillator thickness is given in mm

Chapter 4

Discussion

The results obtained during the analysis will hereby be critically discussed, reviewing the accordance between the theory and the experiment.

4.1 Behaviour of sensitivity

The sensitivity behaviour, as shown in *Figure [3.1]*, clearly decreases as the ratio between the hole diameter and thickness of the collimator decreases. In *Table [2.1]*, in fact, one can appreciate that the more selective collimator is C, while the less selective is A. Varying the source distance, on the other hand, does not influence the sensitivity. This behaviour is expected for a detector equipped with a parallel hole collimator, see *Equation [1.3]*.

4.2 Behaviour of PSF

From *Figure [3.2]*, it is clear that the PSF, for a given collimator, significantly increases only when the source distance increases. This behaviour is obtained by neglecting the visible light produced in the scintillator layer. If the visible light is considered, the PSF also increases when the scintillator thickness increases. This trend is shown in *Figure [3.3]*. This behaviour is perfectly explained by the theory, since the spatial resolution, which is proportional to the PSF, depends on the geometric parameters according to *Equation [1.4]*.

By inspecting *Figures [3.6]-[3.7]* and *Tables [3.8]-[3.9]*, it can be seen that there is direct proportionality between source distance and PSF value. The direct proportionality between PSF and hole diameter to collimator thickness can be observed in *Figures [3.4]-[3.5]* and *Tables [3.6]-[3.7]*, where the angular coefficient, which in the case of *Equation [1.4]* would be equal to $\frac{d}{l}$, increases with decreasing hole diameter to collimator thickness ratio. Furthermore, by inspecting *Tables [3.7]-[3.9]* it can be determined that the effect of visible light produced inside the scintillator layer is an increase in PSF (therefore a degradation in spatial resolution, or "blurring") both for constant distance and constant collimator geometry as the scintillator layer's thickness increases. In table *Tables [3.7]* an increase in scintillator thickness induces an appreciable increase in the angular coefficient only when it reaches at least 10 mm since then the light will be spreading more before reaching the end of the

detector and its spreading is less significant for smaller thicknesses.

4.3   On the rejected simulations

In *Tables [3.3]-[3.2]* one can appreciate the number of simulations rejected and, considering that a total of 10 simulation for each configuration was performed, that quantity of rejected simulations is significant. We will now propose our hypothesis that, when considered concurrently, may explain this behaviour behaviour.

4.3.1   Barlett's Test Sensitivity

As mentioned in *Appendix [B]*, Barlett's test is sensitive to normality departures. Visual inspection of the distribution of interaction positions on both axis arises some suspicions about their normality, particularly the one refferring to the y axis. In fact, by inspecting *Tables [A.3]-[A.4]*, where the average of the rejected FWHM is presented, it can be seen that some rejections, for instance the one in the third column of the first row, appear to be particularly harsh: the rejection could be due a more or less severe deviation from normality on the y axis due to the various observable peaks in the interaction positions' distribution combined with it's sharpness.
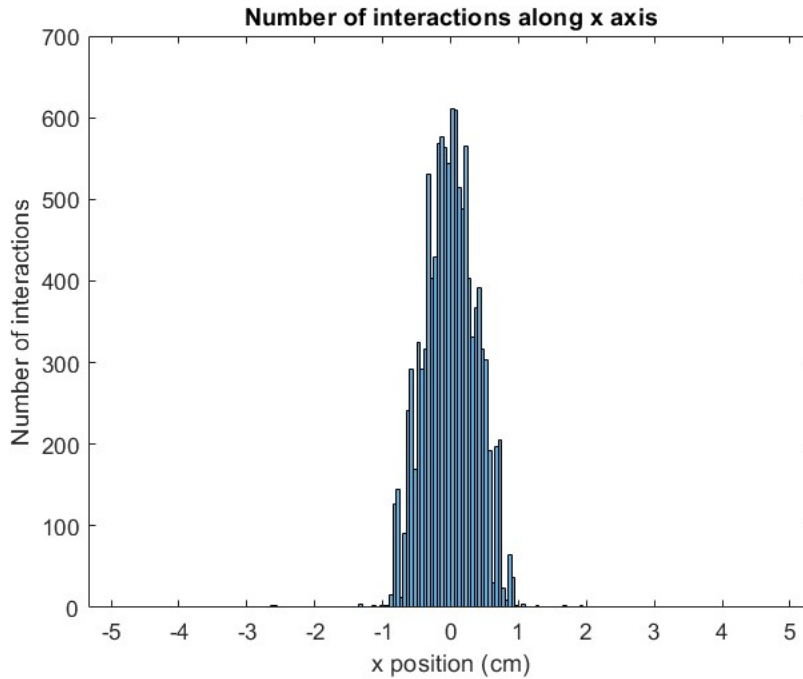

Figure 4.1: Histogram of the x axis interaction positions in one of the rejected simulations belonging to the 5 cm, 2 mm C geometry configuration
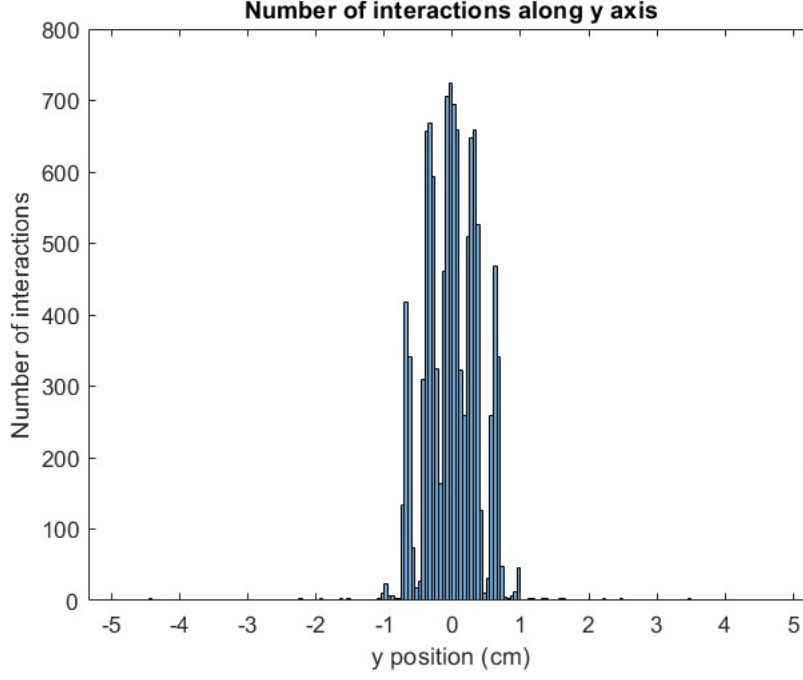
Figure 4.2: Histogram of the y axis interaction positions in one of the rejected simulations belonging to the 5 cm, 2 mm C geometry configuration

4.3.2 Collimator Geometry

The geometry of the collimator, being an hexagonal grid, might induce more anisotropy than previously estimated. This can be seen by comparing *Figures [4.1]* and *[4.2]*: the fact that the prominent peaks are present only on the y axis histogram might be a symptom of it.

Appendix A

Additional tables

A.1 p-values

	A	B	C
2 mm - 5 cm	0.40	0.45	0.16
10 mm - 5 cm	0.32	0.48	0.23
2 mm - 10 cm	0.51	0.54	0.45
10 mm - 10 cm	0.50	0.50	0.57
2 mm - 15 cm	0.59	0.67	0.57
10 mm - 15 cm	0.59	0.51	0.48

Table A.1: Mean p-values for the Barlett's test performed as discussed in section 2.3, performed for each combination of collimator geometry (Table 2.1) source distance and scintillator thickness, while not taking into consideration the blurring induced by the visible light. Scintillator thickness is reported in mm while source distance is reported in cm.

	A	B	C
2 mm - 5 cm	0.52	0.47	0.19
10 mm - 5 cm	0.38	0.60	0.42
2 mm - 10 cm	0.52	0.55	0.46
10 mm - 10 cm	0.52	0.55	0.50
2 mm - 15 cm	0.56	0.70	0.58
10 mm - 15 cm	0.42	0.60	0.52

Table A.2: Reads as *Table [A.1]*, but filled using p-values computed from the position distributions which take into account the blurring caused by visible light.

A.2 Anisotropic FWHM means and std

	A $FWHM_x$, $FWHM_y$	B $FWHM_x$, $FWHM_y$	C $FWHM_x$, $FWHM_y$
2 mm - 5 cm	(1.630±0.003),(1.658±0.005)	(1.257±/),(1.238±/)	(0.98±0.01),(0.97±0.02)
10 mm - 5 cm	(1.638±/),(1.669±/)	(1.241±/),(1.223±/)	(0.95±0.01),(0.95±0.02)
2 mm - 10 cm	(2.707±/),(2.675±/)	-	(1.583±/),(1.552±/)
10 mm - 10 cm	(2.670±/),(2.610±/)	(2.085±/),(2.120±/)	-
2 mm - 15 cm	-	-	-
10 mm - 15 cm	-	(2.992±/),(2.953±/)	(2.151±/),(2.106±/)

Table A.3: Mean and standard deviation values for the FWHM calculated using the standard on the x and y axis for simulation results deemed non-isotropic when not considering the effect of visible light. When the standard deviation is not computable it is substituted by "/" and configurations which have found no non-isotropic results are denoted by -

	A $FWHM_x$, $FWHM_y$	B $FWHM_x$, $FWHM_y$	C $FWHM_x$, $FWHM_y$
2 mm - 5 cm	(1.636±0.003),(1.664±0.006)	(1.264±/),(1.245±/)	(0.99±0.01),(0.98± 0.02)
10 mm - 5 cm	(1.809±/),(1.846±/)	(1.456±/),(1.476±/)	(1.21±0.02),(1.240±0.008)
2 mm - 10 cm	(2.711±/),(2.678±/)	-	(1.589±/),(1.558±/)
10 mm - 10 cm	(1.630 ± 0.003),(1.658 ± 0.005)	(1.630 ± 0.003),(1.658 ± 0.005)	(1.630 ± 0.003),(1.658 ± 0.005)
2 mm - 15 cm	(2.778±/),(2.823±/)	(2.219±/),(2.255±/)	-
10 mm - 15 cm	-	-	(2.284±/),(2.235±/)

Table A.4: Reads as *Table [A.3]*, but filled using FWHM computed from the position distributions which take into account the blurring caused by visible light.

Appendix B

Barlett's Test

Barlett's test verifies homoscedasticity (equality of variance) between the populations from which samples are extracted. Given $k \geq 2$ samples the null-hypothesis is that all the k samples come from populations which have equal variance and the alternative hypothesis is that at least two have different variances. The test, given that n_i and S_i^2 are respectively the size and sample variance of the ith sample, is performed by computing the following:

$$\chi^2 = \frac{(N-k)\ln S_p^2 - \sum_{i=1}^{k}(n_i - 1)\ln S_i^2}{1 + \frac{1}{3(k-1)}\left(\sum_{i=1}^{k}\left(\frac{1}{n_i-1}\right) - \frac{1}{N-k}\right)}$$

where $N = \sum_{i=1}^{k} n_i$ is the total number of measures and $S_p^2 = \frac{1}{N-k}\sum_{i=1}^{k}(n_i - 1)S_i^2$ is the pooled variance, used to estimate the variance of different populations which means may differ. the χ variable when computed as such follows the χ^2 distributions with $k-1$ degrees of freedom. When the likelihood (p-value) of obtaining the estimated χ^2 is lower than a predetermined amount ($p = 0.05$, in the context of this work) then the null-hypothesis is rejected. It is important to note that the test is sensitive to departures from normality [2].

Bibliography

[1] Boone, J.B.S.L.J.: The essential physics of medical imaging 3rd edition. Lippincott Williams (2012)

[2] Box, G.E.P.: Non-normality and tests on variances. Biometrika (1953)

[3] Snedecor, G.W., Cochran, W.G.: Statistical methods, eighth edition. Iowa State University Press ISBN 978-0-8138-1561-9 (1989)